PROCEEDINGS A

rspa.royalsocietypublishing.org

Research

Check for updates

Cite this article: Serra M, Haller G. 2017 Efficient computation of null geodesics with applications to coherent vortex detection. *Proc. R. Soc. A* **473**: 20160807. http://dx.doi.org/10.1098/rspa.2016.0807

Received: 29 October 2016
Accepted: 3 February 2017

Subject Areas:
applied mathematics, fluid mechanics, differential equations

Keywords:
coherent vortices, transport, geodesic flows, closed null geodesics, ocean surface flows

Author for correspondence:
George Haller
e-mail: georgehaller@ethz.ch

Efficient computation of null geodesics with applications to coherent vortex detection

Mattia Serra and George Haller

Institute for Mechanical Systems, ETH Zürich, Leonhardstrasse 21, 8092 Zürich, Switzerland

MS, 0000-0002-6007-5878

Recent results suggest that boundaries of coherent fluid vortices (elliptic coherent structures) can be identified as closed null geodesics of appropriate Lorentzian metrics defined on the flow domain. Here we derive an automated method for computing such null geodesics based on the geometry of the underlying geodesic flow. Our approach simplifies and improves existing procedures for computing variationally defined Eulerian and Lagrangian vortex boundaries. As an illustration, we compute objective vortex boundaries from satellite-inferred ocean velocity data. A MATLAB implementation of our method is available at https://github.com/MattiaSerra/Closed-Null-Geodesics-2D.

1. Introduction

Typical trajectories of general unsteady flows show complex paths, yet their phase space often contains regions of organized behaviour. In light of this, several methods for the identification of coherent structures (CSs) have been developed [1–6]. Only recent mathematical results [7–12], however, offer a rigorous and objective (frame-invariant) definition of CSs, uncovering the skeletons behind these well-organized regions.

Objective coherent structures (OCSs) can be classified as Lagrangian coherent structures (LCSs) and objective Eulerian coherent structures (OECSs), depending on the time interval over which they organize nearby trajectories. Specifically, LCSs [13] are influential over a finite time interval, while OECSs [12] are infinitesimally short-term limits of LCSs. LCSs are suitable for understanding and quantifying finite-time transport and mixing in fluid flows, intrinsically tied to a preselected time interval.

THE ROYAL SOCIETY PUBLISHING

OECSs, by contrast, can be computed at any time instant, and hence are free from any assumptions on time scales. They are, therefore, promising tools for flow-control and real-time decision-making problems [14]. Among the different types of coherent structures, vortex-type (elliptic) structures are perhaps the most relevant for transport prediction and estimation, as they carry the same fluid mass without filamentation or stretching over extended distances.

Lagrangian coherent vortices, in the sense of [9], are encircled by elliptic LCSs, i.e. exceptional material barriers that exhibit no appreciable stretching or folding over a finite time interval. By contrast, Eulerian coherent vortex boundaries (elliptic OECSs), in the sense of [12], are the instantaneous limits of elliptic LCSs. As such, elliptic OECSs are distinguished curves characterized by a lack of short-term filamentation. We will refer to elliptic LCSs and elliptic OECSs collectively as elliptic OCSs. An alternative method for the identification of Lagrangian coherent vortices can be found in [15]. Specifically, the method devised in [15] computes vortex boundaries as stationary curves of the underlying stretching-based variational problem numerically, as opposed to [9], in which the variational problem is solved exactly.

Variational arguments show that elliptic OCSs can be located as null geodesics of suitably defined Lorentzian metrics [9,12]. Their computation, however, requires a number of non-standard steps that complicate its implementation. These steps include (i) an accurate computation of eigenvalues and eigenvectors of tensor fields [16]; (ii) trajectory integration for direction fields as opposed to vector fields [17]; (iii) detection of singularities (regions of repeated eigenvalues) of tensor fields and identification of their topological type [8]; and (iv) selection of Poincaré sections (PSs) for locating closed direction-field trajectories (see [18] or appendix A).

We develop here a simple and accurate method for the computation of closed null geodesics in two dimensions as periodic solutions of the initial value problem

$$\left.\begin{aligned} r' = \mathcal{F}(r, A(r), \nabla A(r)),\ r := \begin{bmatrix} x \\ \phi \end{bmatrix} \in U \times \mathbb{S}^1,\ U \subset \mathbb{R}^2,\ \mathbb{S}^1 := [0, 2\pi) \\ \text{and} \qquad r(0) \in \mathcal{R}_0, \end{aligned}\right\} \tag{1.1}$$

where $\mathcal{F}(r, A, \nabla A)$ denotes a three-dimensional vector field, x denotes the parametrization of the null geodesic, ϕ denotes the angle enclosed by its tangent direction and the horizontal axis, and $A \in \mathbb{R}^{2\times 2}$ denotes the metric tensor associated with the particular type of elliptic OCSs. Based on the topological properties of planar closed curves, we also derive the set of admissible initial conditions $\mathcal{R}_0$ for null geodesics. Seeking periodic orbits of the initial value problem (1.1) is a significant simplification over previous approaches that were designed to locate closed null geodesics as closed orbits of non-orientable direction fields with a large number of singularities ([9,18] or appendix A). Specifically, Karrasch *et al.* [18] devised an automated scheme for the detection of closed null geodesics that relies on locating tensor-field singularities [19], and requires user-input parameters (see appendix A). Furthermore, the detection of such singularities is a sensitive process. This sensitivity increases with the integration time, leading to artificial clusters of singularities (see [18] or figure 6), which in turns precludes the detection of the outermost coherent vortex boundaries. Our method overcomes these limitations and identifies closed null geodesics of a general Lorentzian metric without restrictions on their geometry, or on the number and type of singularities present in their interior (cf. figure 7).

The global orientability of $\mathcal{F}(r, A, \nabla A)$ also allows for cubic or spline interpolation schemes. This leads to more accurate computations than with the integration of direction fields, for which the lack of global orientability necessitates the use of linear interpolation. These simplifications enable a fully automated and accurate detection of variationally defined vortex boundaries in any two-dimensional unsteady velocity field without reliance on user inputs. The integration of the three-dimensional vector field (1.1), as well as the computation of the admissible set of initial conditions $\mathcal{R}_0$, uses standard built-in MATLAB functions available as supplementary material to this paper (see §7). Finally, the ODE in (1.1) can be used to compute null geodesics of general Lorentzian metrics, and hence is also relevant for hyperbolic and parabolic OCSs defined from variational principles in [8,12].

2. Formulation of the problem

We consider a variational problem

$$Q[\gamma(s)] = \int_\gamma L(x(s), x'(s))\,\mathrm{d}s \quad \text{and} \quad \delta \int_\gamma L(x(s), x'(s))\,\mathrm{d}s = 0, \tag{2.1}$$

with a quadratic Lagrangian

$$L(x, x') = \tfrac{1}{2}\langle x', A(x)x'\rangle, \tag{2.2}$$

where $A(x)$ is a tensor for all $x \in U \subset \mathbb{R}^2$, and $\langle\cdot,\cdot\rangle$ denotes the Euclidean inner product. Let $x : s \mapsto x(s),\ s \in [0, \sigma] \subset \mathbb{R}$, denote the parametrization of a geodesic γ of the metric

$$g_x(x', x') = \tfrac{1}{2}\langle x', A(x)x'\rangle \tag{2.3}$$

and $x'(s) := \mathrm{d}x/\mathrm{d}s$ its local tangent vector.

The Euler–Lagrange equations [20] associated with (2.1) are

$$\frac{1}{2}\nabla_x\langle x', A(x)x'\rangle - \frac{\mathrm{d}}{\mathrm{d}s}[A(x)x'] = 0$$

with the equivalent four-dimensional first-order formulation

$$\left.\begin{aligned} & x' = v \\ \text{and} \quad & v' = \tfrac{1}{2}A^{-1}(x)[\nabla_x\langle x', A(x)x'\rangle] - A^{-1}(x)[(\nabla_x A(x)v)v]. \end{aligned}\right\} \tag{2.4}$$

Here, in tensor notation and with summation implied over repeated indices,

$$v_i' = \tfrac{1}{2}A_{ij}^{-1}(x)v_k A_{kl,j}(x)v_l - A_{ij}^{-1}A_{jk,l}(x)v_l v_k, \quad i, j, k, l \in \{1, 2\}.$$

The functional $L(x, x')$ in (2.2) has no explicit dependence on the parameter s. By Noether's theorem [20], the metric $g_x(v, v)$ is a first integral for (2.4), i.e.

$$g_{x(s)}(v(s), v(s)) = \tfrac{1}{2}\langle v(s), A(x(s))v(s)\rangle = g_0 = \text{const.} \tag{2.5}$$

Any non-degenerate level surface satisfying $g_x(v, v) = g_0$ defines a three-dimensional invariant manifold for (2.4) in the four-dimensional space coordinatized by (x, v). Differentiation with respect to s along trajectories in this manifold gives

$$\frac{\mathrm{d}g_x}{\mathrm{d}s} = \langle \nabla_{(x,v)} g_{x(s)}(v(s), v(s)), (x', v')\rangle = 0,$$

which is equivalent to

$$\begin{aligned} 2\langle v', A(x)v\rangle &= -\langle v, (\nabla_x A(x)v)v\rangle, \\ &= -v_i A_{ij,k}(x)v_k v_j, \quad i, j, k \in \{1, 2\}. \end{aligned} \tag{2.6}$$

We denote with $(\cdot)_\parallel$ and $(\cdot)_\perp$ the components of $(\cdot)$ along v and $v^\perp = Rv$, respectively, where R is a counterclockwise 90° rotation matrix. Expressing $v' = v_\parallel' + v_\perp'$, we rewrite equation (2.6) as

$$2\langle v_\parallel', A(x)v\rangle + 2\langle v_\perp', A(x)v\rangle = -\langle v, (\nabla_x A(x)v)v\rangle. \tag{2.7}$$

Of particular interest for us are null geodesics of $g_x(v, v)$. Such curves satisfy $g_x(v, v) \equiv 0$. In this case, equation (2.7) simplifies to

$$2\langle v_\perp', A(x)v\rangle = -\langle v, (\nabla_x A(x)v)v\rangle. \tag{2.8}$$

Geometrically, this means that null geodesics on (U, g_x) do not depend on their parametrization, only on their geometry. Equation (2.8) holds in any dimension ($x \in \mathbb{R}^n$), but we keep our discussion two dimensional to focus on coherent-structure detections in planar flows.

3. Reduced three-dimensional null-geodesic flow

(a) Flow reduction

We introduce polar coordinates in the v direction by letting

$$v = \rho e_\phi, \quad \rho \in \mathbb{R}^+, \quad e_\phi = (\cos\phi, \sin\phi)^\top, \quad \phi \in \mathbb{S}^1 \tag{3.1}$$

and rewrite equation (2.5) along null geodesics as

$$g_x(\rho e_\phi, \rho e_\phi) = \rho^2 g_x(e_\phi, e_\phi) = g_0 \equiv 0 \iff \tfrac{1}{2}\langle e_\phi, A(x) e_\phi\rangle = 0, \quad x \in U,\ \phi \in \mathbb{S}^1. \tag{3.2}$$

We also define the zero surface of g_x as

$$\mathcal{M} = \{(x,\phi) \in U \times \mathbb{S}^1 : g_x(e_\phi, e_\phi) = \tfrac{1}{2}\langle e_\phi, A(x)e_\phi\rangle = 0\}. \tag{3.3}$$

In addition, we rewrite equation (2.8) as

$$2\phi'\langle Re_\phi, A(x)e_\phi\rangle = -\rho\langle e_\phi, (\nabla_x A(x)e_\phi)e_\phi\rangle, \quad R := \begin{pmatrix} 0 & -1 \\ 1 & 0 \end{pmatrix} \tag{3.4}$$

or, equivalently,

$$\left.\begin{aligned} x' &= \rho e_\phi \\ \text{and} \qquad \phi' &= -\rho \frac{\langle e_\phi, (\nabla_x A(x)e_\phi)e_\phi\rangle}{2\langle e_\phi, R^\top A(x)e_\phi\rangle}. \end{aligned}\right\} \tag{3.5}$$

Next, we rescale time along each trajectory $(x(s), \rho(s), \phi(s))$ of (3.5) by letting

$$\bar{s} = \int_0^s \rho(\sigma)\,\mathrm{d}\sigma, \tag{3.6}$$

which gives $\mathrm{d}x/\mathrm{d}\bar{s} = e_\phi$, $\mathrm{d}\phi/\mathrm{d}\bar{s} = -\langle e_\phi, (\nabla_x A(x)e_\phi)e_\phi\rangle / 2\langle e_\phi, R^\top A(x)e_\phi\rangle$. We then drop the bar on s to obtain the final form

$$\left.\begin{aligned} \frac{\mathrm{d}x}{\mathrm{d}s} &= e_\phi \\ \text{and} \qquad \frac{\mathrm{d}\phi}{\mathrm{d}s} &= -\frac{\langle e_\phi, (\nabla_x A(x)e_\phi)e_\phi\rangle}{2\langle e_\phi, R^\top A(x)e_\phi\rangle}, \end{aligned}\right\} \tag{3.7}$$

for the reduced three-dimensional null-geodesic flow, which is defined on the set

$$V = \{(x,\phi) \in U \times \mathbb{S}^1 : A(x)e_\phi \nparallel e_\phi,\ A(x) \neq \mathbf{0}\},$$

where $\mathbf{0} \in \mathbb{R}^{2\times 2}$ denotes the null tensor (see appendix C). In words, V is the set of points in $U \times \mathbb{S}^1$ where $A(x)$ is non-degenerate and e_ϕ is not aligned with the eigenvectors of $A(x)$. Note that, by construction, $\phi'(s)$ is the pointwise curvature of γ. An equation related to equation (3.7) appears in [21] for the geodesic flow associated with the Riemannian metric on a general manifold, defined as the zero set of a smooth function $F(x)$.

As a consequence of equations (2.7) and (2.8), the ODE (3.7) has one dimension less than equation (2.4), and the x-projection of its integral curves coincides with null geodesics on (U, g_x). This follows from the equivalence of null surfaces and null geodesics in two dimensions. In appendix D, using the Hamiltonian formalism, we derive an equivalent reduced geodesic flow in the (x, p) variables, with p denoting the generalized momentum.

Figure 1 shows a closed null geodesic γ of the metric $g_x(v, v)$ both in the x-subspace (figure 1*a*) and in the $U \times \mathbb{S}^1$-space (figure 1*b*). Specifically, figure 1*b* shows a closed integral curve of (3.7) on the manifold $\mathcal{M}$.

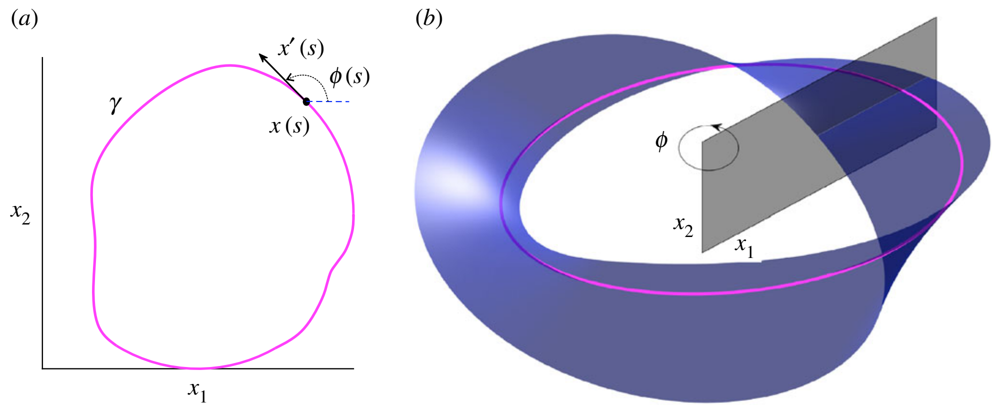

Figure 1. (*a*) Closed null geodesic of $g_x(v, v)$ in the x-subspace. (*b*) Closed null geodesic of $g_x(u, u)$ in $U \times \mathbb{S}^1$ on the zero-level surface of $g_x(e_\phi, e_\phi)$. In this space, a closed null geodesic is an integral curve of (3.7) satisfying the boundary conditions: $x(\sigma) = x(0)$ and $\phi(\sigma) = \phi(0) \pm 2\pi$. (Online version in colour.)

(b) Dependence on parameters

In applications to coherent vortex detection (see §4), the tensor field $A(x)$ depends on a parameter $\alpha \in \mathbb{R}$, leading to a specific Lorentzian metric family of the form

$$g_{x,\alpha} = \tfrac{1}{2}\langle v, A_\alpha(x)v\rangle, \quad A_\alpha = A(x) - \alpha I. \tag{3.8}$$

The zero-level set of the metric family is defined by $g_{x,\alpha}(e_\phi, e_\phi) = 0$. Interestingly, however, plugging formula (3.8) into equation (3.7), we find out that the reduced ODE (3.7) remains independent of α, i.e.

$$\frac{\langle e_\phi, (\nabla_x A_\alpha(x)e_\phi)e_\phi\rangle}{2\langle e_\phi, R^\top A_\alpha(x)e_\phi\rangle} = \frac{\langle e_\phi, (\nabla_x A(x)e_\phi)e_\phi\rangle}{2\langle e_\phi, R^\top A(x)e_\phi\rangle}. \tag{3.9}$$

This is because $\nabla_x \alpha I = 0$ as αI does not depend on x, and $\langle e_\phi, \alpha R^\top I e_\phi\rangle = 0$ because $R^\top I$ is skew-symmetric. We summarize this result in the following theorem.

Theorem 3.1. *The reduced three-dimensional null-geodesics flow of the Lorentzian metric family $g_{x,\alpha}(v, v) = \frac{1}{2}\langle v, A_\alpha(x)v\rangle$, $A_\alpha(x) = A(x) - \alpha I$, $\alpha \in \mathbb{R}$, is independent of α and satisfies the differential equation*

$$\begin{aligned} x' &= e_\phi, \\ \phi' &= -\frac{\langle e_\phi, (\nabla_x A(x)e_\phi)e_\phi\rangle}{2\langle e_\phi, R^\top A(x)e_\phi\rangle}, \end{aligned}$$

defined on the set

$$V = \{(x, \phi) \in U \times \mathbb{S}^1 : A(x)e_\phi \nparallel e_\phi, \ A(x) \neq \mathbf{0}\}.$$

The ODE (3.7) is independent of α, and hence all null geodesics of the metric family $g_{x,\alpha}$ can be integrated under the same vector field, as opposed to available direction-field formulations that depend on α (see appendix A, equation (A 1)). This property of the ODE (3.7) further simplifies the computation of null geodesics of $g_{x,\alpha}(v, v)$.

(c) Initial conditions for closed null geodesics

The only missing ingredient for computing closed null geodesics of $g_{x,\alpha}$ is a set of initial conditions for the reduced null-geodesic flow (3.7). Here we derive the set of initial conditions $\mathcal{R}_0 \subset V$, such that any closed null geodesic of $g_{x,\alpha}$ necessarily contains a point in $\mathcal{R}_0$. According to §§2 and 3,

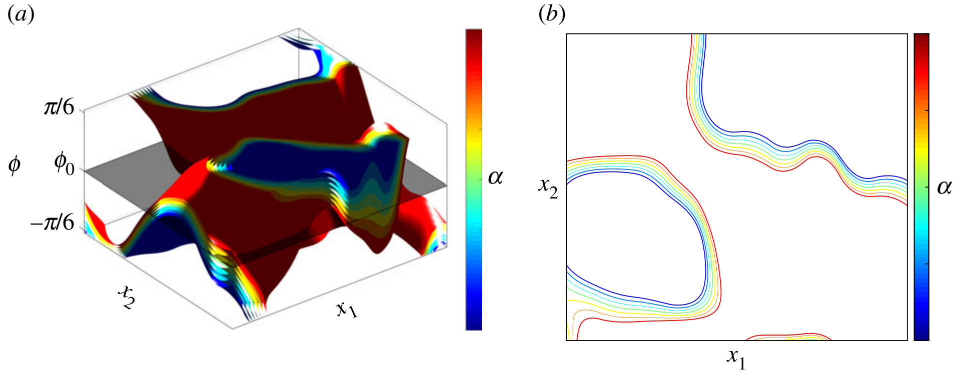

Figure 2. (*a*) Section ($\phi \in [-\pi/6, \pi/6]$) of $\mathcal{M}_\alpha$ for different values of α, in a flow example analysed in more detail in §5. The black plane corresponds to $\phi(x) = \phi_0 = 0$. (*b*) Set of points $x_0(\alpha, \phi_0) \in U$ satisfying $g_{x_0,\alpha}(e_0, e_0) = 0$, i.e. $\mathcal{M}_\alpha \cap \phi(x) = \phi_0 = 0$, for different values of α. (Online version in colour.)

for any fixed value of α, null geodesics of $g_{x,\alpha}$ must lie on the zero-level surface of $g_{x,\alpha}(e_\phi, e_\phi)$, i.e. on

$$\mathcal{M}_\alpha = \{(x, \phi) \in U \times \mathbb{S}^1 : g_{x,\alpha}(e_\phi, e_\phi) = 0\}.$$

Furthermore, for every closed planar curve γ, the angle ϕ between its local tangent vector and an arbitrary fixed direction (figure 1*a*) assumes all values in the interval $[0, 2\pi]$. This simple topological property of closed regular planar curves allows us to define the admissible set of initial conditions for (3.7) as follows.

For any fixed $\alpha \in \mathbb{R}$ and any fixed $\phi_0 \in \mathbb{S}^1$, we compute the set of initial conditions $\mathcal{R}_{\alpha,\phi_0}(0)$ as

$$\mathcal{R}_{\alpha,\phi_0}(0) = \{(x_0(\alpha, \phi_0), \phi_0) \in V : g_{x_0,\alpha}(e_{\phi_0}, e_{\phi_0}) = 0\}. \tag{3.10}$$

Figure 2 illustrates formula (3.10) in a flow example analysed in more detail in §5. Specifically, figure 2*a* shows a section ($\phi \in [-\pi/6, \pi/6]$) of $\mathcal{M}_\alpha$ for different values of α. The $\phi(x) = \phi_0 = 0$ plane is shown in black. Figure 2*b* shows the set points $x_0(\alpha, \phi_0) \in U$ satisfying $g_{x_0,\alpha}(e_0, e_0) = 0$. For any fixed α, the points within the set of initial conditions $\mathcal{R}_{\alpha,\phi_0}(0)$ that lie on closed null geodesics are the ones for which the reduced ODE (3.7) admits a closed orbit (see, for example, the green dot in the inset of figure 3*c*).

(d) The initial value problem for closed null geodesics

Putting together the results from §3, we obtain our main result, already summarized briefly in equation (1.1).

Theorem 3.2. *For any fixed parameter value $\alpha \in \mathbb{R}$, and any fixed $\phi_0 \in \mathbb{S}^1$, define the set of initial conditions*

$$(x_0, \phi_0)_\alpha = \{(x_0(\alpha, \phi_0), \phi_0) \in V : \tfrac{1}{2}\langle e_{\phi_0}, (A(x_0) - \alpha I)e_{\phi_0}\rangle = 0\}. \tag{3.11}$$

Closed null geodesics of the Lorentzian metric family $g_{x,\alpha}(v, v) = \frac{1}{2}\langle v, A_\alpha(x)v\rangle$, $A_\alpha(x) = A(x) - \alpha I$, coincide with the x-projection of closed orbits of the initial value problem

$$\left.\begin{aligned} x' &= e_\phi, \\ \phi' &= -\frac{\langle e_\phi, (\nabla_x A(x) e_\phi) e_\phi\rangle}{2\langle e_\phi, R^\top A(x) e_\phi\rangle} \\ \text{and} \quad x(0) &= x_0(\alpha, \phi_0), \quad \phi(0) = \phi_0 \end{aligned}\right\} \tag{3.12}$$

defined for any parameter value $\alpha \in \mathbb{R}$ on the set

$$V = \{x \in U,\ \phi \in \mathbb{S}^1 : \langle e_\phi, R^\top A(x) e_\phi\rangle \neq 0\}. \tag{3.13}$$

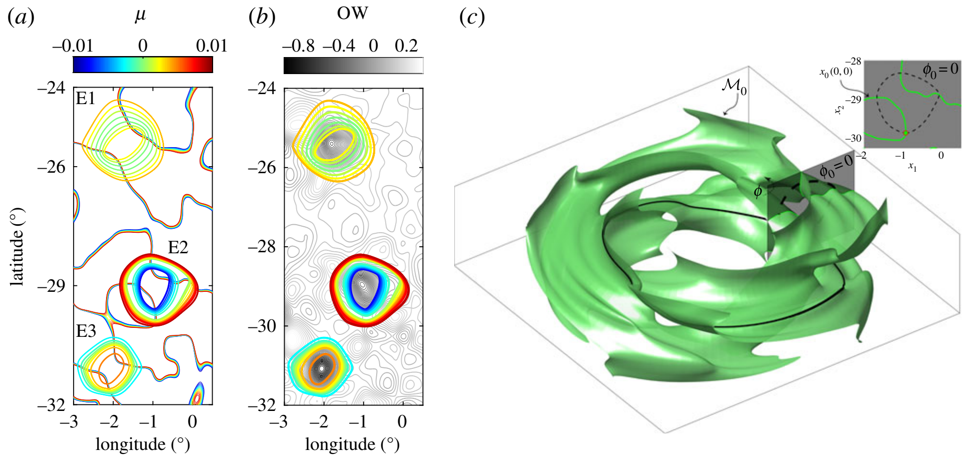

Figure 3. (*a*) Elliptic OECSs for different values of the stretching rate μ (in colour) along with the x-component of the initial conditions $x_0(\mu, 0)$, as defined in equation (4.12). (*b*) The same elliptic OECSs as (*a*) on level sets of the OW parameter encoded with the grey colour map. (*c*) Elliptic OECS for $\mu = 0$ corresponding to the vortical region denoted by E2 (see (*a*)) in the $\mathbb{R}^2 \times \mathbb{S}^1$ space. The green surface represents the zero set defined by equation (4.9), the green curves show the set of initial conditions $(x_0(0, 0), 0)$ computed with equation (4.12), the solid black curve is the periodic orbit of the ODE (4.11) with initial and final points represented by the green dot and the red circle, respectively. The dashed black curve is the corresponding elliptic OECSs. (Online version in colour.)

Null geodesics for a given value of α *lie on the zero-level surface of* $g_{x,\alpha}(e_\phi, e_\phi)$ *defined as*

$$\mathcal{M}_\alpha = \{(x, \phi) \in V : \tfrac{1}{2}\langle e_\phi, (A(x) - \alpha I)e_\phi\rangle = 0\}. \tag{3.14}$$

For any fixed valued of α, the surface $\mathcal{M}_\alpha$ is a graph of the form $\phi(x, \alpha)$. Differentiating now $g_{x,\alpha}(e_{\phi(x,\alpha)}, e_{\phi(x,\alpha)})$ with respect to α, we obtain $\partial_\alpha \phi(x, \alpha) = \langle e_\phi, R^\top A(x)e_\phi\rangle^{-1}$. This result, together with (3.13), implies that closed null geodesics of $g_{x,\alpha}$ cannot intersect for different values of α, in agreement with the findings of [9,12]. Finally, closed null geodesics on $(U, g_{x,\alpha})$ are structurally stable structures, and hence will persist under small perturbations to $g_{x,\alpha}$. In the case of OCS detection (see §4), therefore, elliptic OCS persist under small perturbation (e.g. noise) to the velocity field (4.1). In the following applications of theorem 3.2, we select $\phi_0 = 0$ in formula (3.11).

4. Null geodesics and the computation of objective coherent structures

In the next section, we recall the terminology used for the definition of LCSs [13] and OECSs [12] in two-dimensional flows. Variational definitions of LCSs are now available also for three-dimensional flows [11], but these definitions do not lead to geodesic problems, and hence are not covered by the computational approach developed here. A similar conclusion holds for OECS definitions obtained as short-term limits of three-dimensional LCS definitions.

(a) Set-up and notation

Consider the two-dimensional non-autonomous dynamical system

$$\dot{x} = u(x, t), \tag{4.1}$$

with a twice continuously differentiable velocity field $u(x, t)$ defined over the open flow domain $U \subset \mathbb{R}^2$, over a time interval $t \in [a, b]$. We recall the customary velocity gradient decomposition

$$\nabla u(x, t) = S(x, t) + W(x, t),$$

Table 1. Lorentzian metrics whose null geodesics define various coherent structures [12,13].

type of OCS	metric: $g(v,v)=\langle v,Av\rangle$ LCS	OECS
hyperbolic and parabolic	$A=\frac{1}{2}[C_{t_0}^t R - RC_{t_0}^t]$	$A=2SR$
elliptic	$A_\lambda=\frac{1}{2}[C_{t_0}^t-\lambda^2 I],\ \lambda\in\mathbb{R}$	$A_\mu=S-\mu I,\ \mu\in\mathbb{R}$

with the rate-of-strain tensor $S=\frac{1}{2}(\nabla u+\nabla u^\top)$ and the spin tensor $W=\frac{1}{2}(\nabla u-\nabla u^\top)$. By our assumptions, both S and W are continuously differentiable in x and t.

The rate-of-strain tensor is objective (i.e. frame indifferent), whereas the spin tensor is not objective, as shown in classic texts on continuum mechanics [22]. The eigenvalues $s_i(x,t)$ and eigenvectors $e_i(x,t)$ of $S(x,t)$ are defined, indexed and oriented here through the relationship

$$Se_i=s_ie_i,\quad |e_i|=1,\ i=1,2;\quad s_1\le s_2,\quad e_2=Re_1.$$

Fluid particle trajectories generated by $u(x,t)$ are solutions of the differential equation $\dot{x}=u(x,t)$, and define the flow map

$$F_{t_0}^t(x_0)=x(t;t_0,x_0),\quad x_0\in U,\quad t\in[t_0,t_1]\subset[a,b],$$

which maps initial particle positions x_0 at time t_0 to their time t positions $x(t;t_0,x_0)$.

The deformation gradient $\nabla F_{t_0}^t$ governs the infinitesimal deformations of the phase space U. In particular, an infinitesimal perturbation ζ_0 at point x_0 and time t_0 is mapped, under system (4.1), to its time t position, $\zeta_t=\nabla F_{t_0}^t(x_0)\zeta_0$. The squared magnitude of the evolving perturbation is governed by

$$\langle\zeta_t,\zeta_t\rangle=\langle\zeta_0,C_{t_0}^t(x_0)\zeta_0\rangle,\quad C_{t_0}^t(x_0)=[\nabla F_{t_0}^t(x_0)]^\top\nabla F_{t_0}^t(x_0),\tag{4.2}$$

where $C_{t_0}^t$ denotes the right Cauchy–Green strain tensor [22]. The eigenvalues $\lambda_i(x_0)$ and eigenvectors $\xi_i(x_0)$ of $C_{t_0}^t(x_0)$ are defined, indexed and oriented here through the relationship

$$C_{t_0}^t(x_0)\lambda_i(x_0)=\lambda_i(x_0)\xi_i(x_0),\quad |\xi_i|=1,\quad i=1,2;\quad \lambda_1\le\lambda_2,\quad \xi_2=R\xi_1.$$

For notational simplicity, we omit the dependence of $\lambda_i(x_0)$ and $\xi_i(x_0)$ on t_0 and t.

Objective coherent structures are defined as stationary curves of objective (frame-invariant) variational principles and can also be viewed as null geodesics of suitably defined Lorentzian metrics, with specific boundary conditions [12,13]. These metrics are summarized in table 1.

Although equation (3.12) can generally be applied to compute all the coherent structures listed in table 1, here we focus on elliptic OCSs. Elliptic OCSs are closed null geodesics of the corresponding Lorentzian metric families shown in table 1. In fluid dynamics terms, elliptic LCSs are exceptionally coherent vortex boundaries that show no unevenness in their tangential deformation. Similarly, elliptic OECSs are exceptionally coherent vortex boundaries that show no infinitesimally short-term unevenness in their tangential deformation. The parameter λ represents the tangential stretching experienced by an elliptic LCS over the time interval $[t_0,t]$, while μ denotes the tangential stretch rate along an elliptic OECS. In the next two sections, applying theorem 3.2 to the Lorentzian metric families A_μ and A_λ, we derive initial value problems (ODEs and initial conditions) for the computation of Eulerian and Lagrangian vortex boundaries.

(b) Elliptic objective Eulerian coherent structures

Elliptic OECSs are closed null geodesics of the one-parameter family of Lorentzian metrics (see table 1)

$$A_\mu(x,t)=S(x,t)-\mu I.$$

We denote by $S^{ij}(x)$ the entry at row i and column j of $S(x,t)$ at a fixed time t, and its derivatives $\partial_{(\cdot)}S^{ij}(x)$ by $S^{ij}_{(\cdot)}(x)$. A direct application of theorem 3.2 leads to the the following result.

At each time t and for a given value of μ, elliptic OECSs satisfy the pointwise condition

$$S^{11}(x,t)\cos^2\phi + S^{12}(x,t)\sin 2\phi + S^{22}(x,t)\sin^2\phi - \mu = 0, \quad (x,\phi)\in V_t, \tag{4.3}$$

with the set V_t defined as

$$V_t = \{x \in U,\ \phi \in \mathbb{S}^1 :\ \sin 2\phi[S^{22}(x,t) - S^{11}(x,t)] + 2\cos 2\phi S^{12}(x,t) \neq 0\}. \tag{4.4}$$

Elliptic OECSs coincide with the x-projection of closed orbits of the initial value problem

$$\left.\begin{aligned} x' &= e_\phi \\ \text{and} \quad \phi' &= -\frac{\cos^2\phi\langle\nabla_x S^{11}(x,t), e_\phi\rangle + \sin 2\phi\langle\nabla_x S^{12}(x,t), e_\phi\rangle + \sin^2\phi\langle\nabla_x S^{22}(x,t), e_\phi\rangle}{\sin 2\phi[S^{22}(x,t) - S^{11}(x,t)] + 2\cos 2\phi S^{12}(x,t)}, \end{aligned}\right\} \tag{4.5}$$

$$(x_0,\phi_0)_\mu = \{(x_0(\mu,0),0) \in V_t :\ S^{11}(x_0) - \mu = 0\}. \tag{4.6}$$

In the case of incompressible flows ($\nabla \cdot u \equiv 0$), equation (4.5) simplifies to

$$\left.\begin{aligned} x' &= e_\phi \\ \text{and} \quad \phi' &= -\frac{[S^{11}_{x_1}(x,t)\cos\phi + S^{11}_{x_2}(x,t)\sin\phi]\cos 2\phi + [S^{12}_{x_1}(x,t)\cos\phi + S^{12}_{x_2}(x,t)\sin\phi]\sin 2\phi}{2[S^{12}(x,t)\cos 2\phi - S^{11}(x,t)\sin 2\phi]}. \end{aligned}\right\} \tag{4.7}$$

(i) Elliptic OECSs: streamfunction formulation

In case the velocity field is derived from a time-dependent streamfunction $\psi(x,t)$, the ODE (4.1) is of the form

$$\left.\begin{aligned} \dot{x}_1 &= -\psi_{x_2}(x_1,x_2,t) \\ \text{and} \quad \dot{x}_2 &= \psi_{x_1}(x_1,x_2,t). \end{aligned}\right\} \tag{4.8}$$

Denoting the partial derivative $\partial_{x_i}\psi(x)$ by $\psi_i(x)$, $i \in \{1,2\}$, we reformulate our results in terms of the time-dependent streamfunction as follows.

For a velocity field generated by the time-dependent streamfunction $\psi(x_1,x_2,t)$, at each time t and for a given value of μ, elliptic OECSs satisfy the pointwise condition

$$\psi_{21}(x,t)\cos 2\phi + \tfrac{1}{2}[\psi_{22}(x,t) - \psi_{11}(x,t)]\sin 2\phi + \mu = 0, \quad (x,\phi)\in V_t, \tag{4.9}$$

within the set V_t defined as

$$V_t = \{x \in U,\ \phi \in \mathbb{S}^1 :\ [\psi_{11}(x,t) - \psi_{22}(x,t)]\cos 2\phi + 2\psi_{21}(x,t)\sin 2\phi \neq 0\}. \tag{4.10}$$

Furthermore, elliptic OECSs coincide with the x-projection of closed orbits of the initial value problem

$$\left.\begin{aligned} x' &= e_\phi \\ \text{and} \quad \phi' &= -\frac{\langle\nabla_x\psi_{21}(x,t), e_\phi\rangle\cos 2\phi + 1/2\langle\nabla_x[\psi_{11}(x,t) - \psi_{22}(x,t)], e_\phi\rangle\sin 2\phi}{[\psi_{11}(x,t) - \psi_{22}(x,t)]\cos 2\phi + 2\psi_{21}(x,t)\sin 2\phi}, \end{aligned}\right\} \tag{4.11}$$

$$(x_0,\phi_0)_\mu = \{(x_0(\mu,0),0) \in V_t :\ \psi_{21}(x_0,t) - \mu = 0\}. \tag{4.12}$$

(c) Elliptic Lagrangian coherent structures

For Lagrangian vortex boundaries (elliptic LCSs), the underlying Lorentzian metric is (see table 1)

$$A_\lambda(x) = C^t_{t_0}(x) - \lambda^2 I.$$

To avoid confusion with the initial conditions of the reduced null-geodesic flow (see equation (3.11)), here we denote the spatial dependence of the Cauchy–Green by x instead of x_0. Applying theorem 3.2 and denoting by $C^{ij}(x)$ the entry at row i and column j of $C_{t_0}^{t}(x)$ we obtain the following result.

For a fixed time interval $[t_0, t_1]$ and for a given value of λ, elliptic LCSs satisfy pointwise the condition

$$C^{11}(x)\cos^2\phi + C^{12}(x)\sin 2\phi + C^{22}(x)\sin^2\phi - \lambda^2 = 0, \quad (x,\phi) \in V, \tag{4.13}$$

within the set V defined as

$$V = \{x \in U,\ \phi \in \mathbb{S}^1 : \sin 2\phi[C^{22}(x) - C^{11}(x)] + 2\cos 2\phi C^{12}(x) \neq 0\}. \tag{4.14}$$

Furthermore, elliptic LCSs coincide with the x-projection of closed orbits of the initial value problem

$$\left.\begin{aligned} x' &= e_\phi \\ \text{and}\qquad \phi' &= -\frac{\cos^2\phi\langle\nabla_x C^{11}(x), e_\phi\rangle + \sin 2\phi\langle\nabla_x C^{12}(x), e_\phi\rangle + \sin^2\phi\langle\nabla_x C^{22}(x), e_\phi\rangle}{\sin 2\phi[C^{22}(x) - C^{11}(x)] + 2\cos 2\phi C^{12}(x)}, \end{aligned}\right\} \tag{4.15}$$

$$(x_0, \phi_0)_\lambda = \{(x_0(\lambda, 0), 0) \in V : C^{11}(x_0) - \lambda^2 = 0\}. \tag{4.16}$$

5. Example: mesoscale coherent vortices in large-scale ocean data

We now use the results of §4 to locate coherent vortex boundaries in a two-dimensional ocean-surface-velocity dataset derived from AVISO satellite altimetry measurements (http://www.aviso.oceanobs.com). The domain of interest is the Agulhas leakage in the Southern Ocean, bounded by longitudes [3° W, 1° E], latitudes [32° S, 24° S] and the time slice we selected corresponds to $t = 24$ November 2006. This dataset has also been used in the vortex detection studies [12,23,24], which provide a benchmark for comparison with the approach developed here.

Under the geostrophic assumption, the ocean surface height measured by satellites plays the role of a streamfunction for surface currents. With h denoting the sea surface height, the velocity field in longitude–latitude coordinates, $[\varphi, \theta]$, can be expressed as

$$\dot{\varphi} = -\frac{g}{R_E^2 f_c(\theta)\cos\theta}\partial_\theta h(\varphi,\theta,t) \quad \text{and} \quad \dot{\theta} = \frac{g}{R_E^2 f_c(\theta)\cos\theta}\partial_\varphi h(\varphi,\theta,t),$$

where $f_c(\theta) := 2\Omega\sin\theta$ denotes the Coriolis parameter, g denotes the constant of gravity, R_E denotes the mean radius of the Earth and Ω denotes its mean angular velocity. The velocity field is available at weekly intervals, with a spatial longitude–latitude resolution of 0.25°. For more detail on the data, see [25].

(a) Elliptic objective Eulerian coherent structures

Applying the results in §4, we obtain three objectively detected vortical regions in the domain under study, each filled with families of elliptic OECSs (figure 3). Figure 3*a* shows elliptic OECSs for different values of stretching rate μ (in colour), along with the x-component of the initial conditions $x_0(\mu, \phi_0)$ for $\phi_0 = 0$ (see equation (4.12) or figure 2). Figure 3*b* shows the same elliptic OECSs of figure 3*a* along with level sets of the Okubo–Weiss (OW) parameter

$$\mathrm{OW}(x,t) = s_2^2(x,t) - \omega^2(x,t),$$

where $\omega(x,t)$ denotes the vorticity. Spatial domains with $\mathrm{OW}(x,t) < 0$ are frequently used indicators of instantaneous ellipticity in unsteady fluid flows [4,6]. The OW parameter, however, is not objective (the vorticity term will change under rotations), and can hence generate both false positives and false negatives in the vortex detection [12].

Figure 3*c* shows the elliptic OECS in correspondence of eddy 2 (figure 3*a*), for $\mu = 0$, in the $\mathbb{R}^2 \times \mathbb{S}^1$ space. Specifically, the green surface represents the zero set described by equation (4.9),

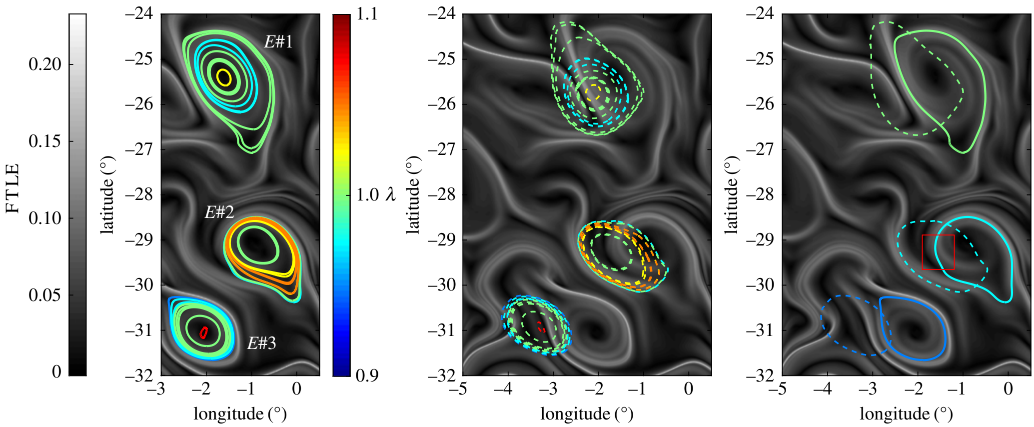

Figure 4. (*a*) Elliptic LCSs for different values of stretching ratio λ (right colour bar) along with the FTLE field at t_0 (left colour bar). (*b*) Advected images of the elliptic LCSs of (*a*) at $t_0 + 30$ days on the FTLE field at t_0. (*c*) Outermost elliptic LCSs of (*a*) (solid lines), together with their corresponding advected images at $t_0 + 30$ days (dashed lines), on the FTLE field at t_0. The red square highlights a region where the local FTLE ridge crosses the elliptic LCS corresponding to eddy 2. (Online version in colour.)

the green curves show the set of initial conditions $(x_0(0, 0), 0)$ computed with equation (4.12), the solid black curve represents the closed integral curve of the ODE (4.11), and the dashed black curve shows the corresponding elliptic OECS, i.e. the x-projection of the solid black curve. The green dot represents the initial condition, within the set $(x_0(0, 0), 0)$, for which the ODE (4.11) admits a closed orbit. The red circle represents the final point of the closed orbit. The domain analysed in figure 3*c* is identical to the one used for illustration in figure 2.

(b) Elliptic Lagrangian coherent structures

In our Lagrangian analysis, we consider the time interval $[t_0, t_0 + T]$, with $t_0 = 24$ November 2006 and $T = 30$ days. Applying the results in §4, we obtain three objectively detected Lagrangian coherent vortices in the domain under study, each filled with families of elliptic LCSs (figure 4).

Figure 4*a* shows elliptic LCSs for different values of the stretching ratio λ (right colour bar), along with the finite-time Lyapunov exponent (FTLE) field

$$\Lambda(x_0, t_0, T) = \frac{1}{2T} \log(\lambda_2(x_0, t_0, t_0 + T)),$$

encoded with the left colour bar. The FTLE measures the maximal local separation of nearby initial conditions over the time interval $[t_0, t_0 + T]$. FTLE ridges are usually used as a visual diagnostic to distinguish coherent regions from the surrounding chaotic regions. The FTLE field, however, does not give any vortex boundary, and can incorrectly indicate the presence of LCSs [13]. Moreover, the extraction of FTLE ridges requires sophisticated post-processing algorithms [26]. This is mainly because ridges separate regions of the phase space with different behaviours, increasing considerably the sensitivity of any numerical computation in their vicinity. Examples include the detection of Cauchy–Green singularities, which plays a crucial role in the direction-field-based procedure for the computation of elliptic LCSs (see appendix A or [18]). Specifically, near FTLE ridges, singularities tend to artificially cluster (figure 6), preventing, possibly, the identification of the outermost elliptic LCSs.

On this note, figure 4*c* shows that the initial positions (solid line) of the outermost elliptic LCSs in correspondence of eddies 1 and 3 almost overlap with nearby FTLE ridges. By contrast, the outermost elliptic LCSs in correspondence of eddy 2 cross the local FTLE ridge (see red square in figure 4*c*). The dashed lines represent the final position of the outermost elliptic LCSs. This highlights two important facts. First, elliptic LCSs computed with the present scheme are insensitive to artificial clusters of singularities, and hence identify the correct boundary of coherent Lagrangian vortices. Second, FTLE ridges do not signal correct Lagrangian vortex boundaries.

Figure 4*b* shows the advected images of elliptic LCSs of figure 4*a* at time $t_0 + 30$ days, along with the FTLE field at t_0. All vortex boundaries remain perfectly coherent for a time interval equal to the extraction time T, as expected.

6. Conclusion

Recently developed variational methods offer exact definitions for OCSs as centrepieces of observed trajectory patterns. OCSs can be classified into LCSs [13] and objective OECSs [12], depending on the time interval over which they shape trajectory patterns. LCSs are intrinsically tied to a specific finite time interval over which they are influential, while OECSs are computable at any time instant, with their influence confined to short time scales. Both types of OCS can be computed as null geodesics of suitably defined Lorentzian metrics defined on the physical domain of the underlying fluid.

Prior numerical procedures for the computation of such vortex boundaries require significant numerical effort to overcome the sensitivity of the steps involved. Here we have derived and tested a simplified and more accurate numerical method. Our method is based on a direct solution of a reduced, three-dimensional version of the underlying ODEs for null geodesics. Based on topological properties of simple planar closed curves, we also derive the admissible set of initial conditions for the reduced ODEs overcoming the limitation of the existing procedure, and making the detection of closed null geodesics fully automated. Specifically, the method we present here does not rely on problem-dependent user-input parameters, and identifies closed null geodesics regardless of the number and type of the metric tensor singularities contained in their interior. In the supplementary material, we provide a MATLAB implementation of this method, with further explanation in appendix B. We have illustrated the present method on mesoscale eddy-boundary extraction from satellite-inferred ocean velocity data.

7. Supplementary material

A MATLAB code for the computation of closed null geodesics is available at https://github.com/MattiaSerra/Closed-Null-Geodesics-2D. Specifically, the MATLAB code computes elliptic LCSs (see §4). Appendix B summarizes the different steps of the main code with explicit references to the different subfunctions.

Data accessibility. The data used in this work are available at http://www.aviso.oceanobs.com. The codes used in this work are available at https://github.com/MattiaSerra/Closed-Null-Geodesics-2D.

Authors' contributions. Both authors contributed equally to this work.

Competing interests. We have no competing interests.

Funding. We received no funding for this study.

Acknowledgements. We acknowledge Alireza Hadjighasem for helpful discussions on the development of the MATLAB code available as the electronic supplementary material.

Appendix A. Direction-field approach for computing elliptic objective coherent structures

Using the notation introduced in §4, we summarize here the direction-field approach for the computation of elliptic LCSs derived in [9]. The initial position of elliptic LCSs coincides with

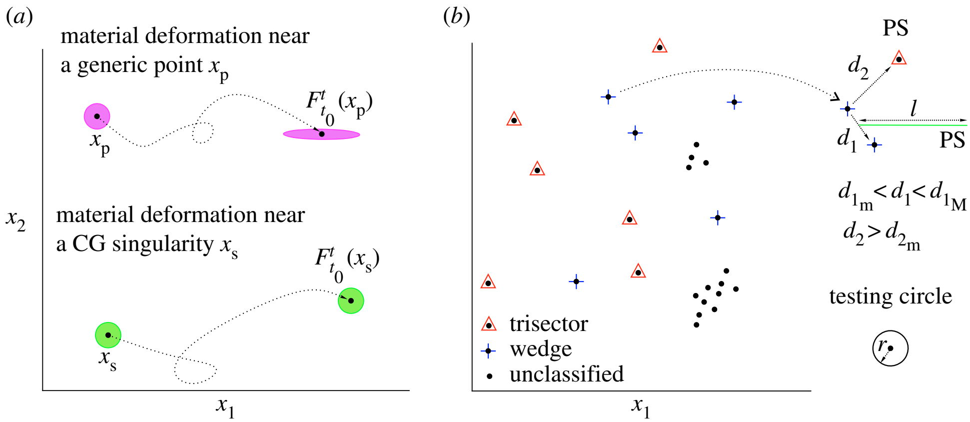

Figure 5. (*a*) Material deformation in the neighbourhood of a generic point x_p, and of a singularity of the Cauchy–Green (CG) tensor x_s, over a finite time interval $[t_0, t]$. (*b*) Identification of the topological type of tensor-line singularities, and definition of the Poincaré section (PS) for the direction-field integration, as in [18]. The user-input parameters $r, l, d_{1_m}, d_{1_M}, d_{2_m}$ are used to locate the PS, and depend on the specific problem. Specifically, r is the radius of the testing circle used to identify the singularity type, l is the length of the PS, and $d_{1_m}, d_{1_M}, d_{2_m}$ bounds the distances of the first two closest singularities from the selected one. (Online version in colour.)

limit cycles of the differential equation family

$$\frac{\mathrm{d}x}{\mathrm{d}s} = \eta_\lambda^\pm(x), \quad \eta_\lambda^\pm = \sqrt{\frac{\lambda_2 - \lambda^2}{\lambda_2 - \lambda_1}}\xi_1 \pm \sqrt{\frac{\lambda^2 - \lambda_1}{\lambda_2 - \lambda_1}}\xi_2. \tag{A 1}$$

The direction fields $\eta_\lambda^\pm(x)$ depend explicitly on λ, and, due to the lack of a well-defined orientation for eigenvector fields, it is *a priori* unknown which one of the $\eta_\lambda^\pm(x)$ fields can have limit cycles. Therefore, both direction fields ($\pm$) should be checked. Similar arguments and expressions hold for elliptic OECSs [12].

(a) Selection of initial conditions

Here we summarize an automated method for the selection of initial conditions (or PSs) of (A 1), developed in [18]. Such a method is based on the location of Cauchy–Green singularities.

Singularities of the Cauchy–Green tensor are exceptional points in the initial configuration of the fluid domain where no distinguished stretching directions exist, and hence an initially circular neighbourhood around them will remain undeformed under the action of the flow map. Figure 5*a* shows the material deformation in the neighbourhood of a generic point x_p, and of a singularity of the Cauchy–Green tensor x_s, over a finite time interval $[t_0, t]$. In a typical turbulent flow, one expects that the occurrence of these points decreases with longer time interval due to the increased mixing in the flow. The detection of tensor-field singularities, however, is a particularly sensitive process, and this sensitivity increases with longer integration times, leading to artificial clusters of singularities (see figure 6 or [18]).

In figure 5*b*, we illustrate the main steps used in [18] to locate the PS for closed null-geodesic computations with the direction-field approach. First, Karrash *et al.* [18] identify the topological type of each singularity using a testing circle of radius r. When singularities are too close to each other (i.e. distance smaller than r), their topological type cannot be identified and they remain unclassified. Applying an index theory argument to direction fields, Karrash *et al.* [18] show that structurally stable singularities contained in the interior of any closed null geodesic on (U, g_x) satisfy the following relation:

$$W = T + 2, \tag{A 2}$$

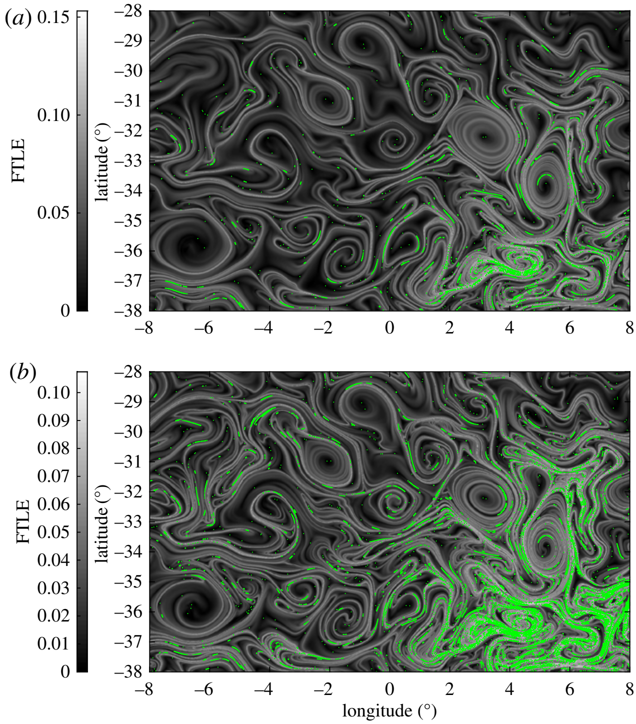

Figure 6. (*a*) Cauchy–Green singularities (green dots) along with the FTLE field for an integration time of two months. (*b*) Cauchy–Green singularities (green dots) along with the FTLE field for an integration time of three months. (Online version in colour.)

where W and T denote the number of wedge-type and trisector-type singularities. Therefore, they conclude that each closed null geodesics contains at least two wedge-type singularities in its interior. Relying on this necessary condition, they seek isolated wedge pairs and set a PS of length l from their mid-points. Specifically, an isolated wedge pair exists if the distance d_1 between the current wedge and the closest one is such that $d_{1_m} < d_1 < d_{1_M}$, and the second closest singularity is a trisector, whose distance $d_2 > d_{2_m}$. This procedure requires user-input parameters $r, l, d_{1_m}, d_{1_M}, d_{2_m}$, which depend not only on the problem but also on the specific region analysed and on the integration time T.

Figure 6 shows the singularities of $C_{t_0}^{t_0+T}(x_0)$ (green dots), along with the corresponding FTLE field, in the flow domain bounded by longitudes [8° W, 8° E], latitudes [38° S, 28° S], with $t_0 =$ 24 November 2006. Specifically, in figure 6*a* the integration time $T = 2$ months, while in figure 6*b* $T = 3$ months. This figure shows an artificial clustering of singularities with increasing integration times, which makes singularity-based methods for detecting closed null geodesics non-optimal.

Even if no such clustering of singularities occurs (e.g. in the detection of elliptic OECSs), a parameter-free method, such as the one developed here, is necessary to avoid all possible false negatives in coherent structure detection. More specifically, the algorithm developed by Karrash *et al.* [18] limits the admissible number of singularities within any closed null geodesic to a maximal number defined by the user. A closed null geodesics not satisfying this condition will not be detected.

As an illustration, figure 7*a* shows elliptic OECSs identified from equations (4.11) and (4.12), in the Southern Ocean (longitudes [3° W, 0° E], latitudes [38° S, 35° S]) at time $t = 24$ November 2006, along with the x-component of the initial conditions $x_0(\mu, 0)$. Figure 7*b* shows the same null geodesics as figure 7*a*, along with the singularities of the underlying tensor field $S(x, t)$. Even though formula (A 2) is satisfied, the automated method proposed in [18] would miss these closed

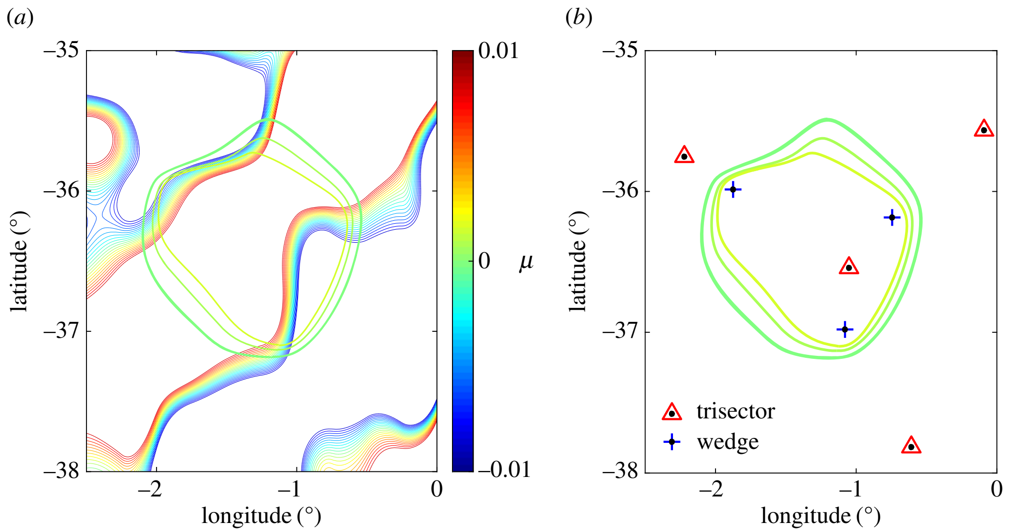

Figure 7. (*a*) Elliptic OECSs for different values of the stretching rate μ (in colour) identified from equations (4.11) and (4.12), in the Southern Ocean (longitudes [3° W, 0° E], latitudes [38° S, 35° S]) at time $t = 24$ November 2006, along with the x-component of the initial conditions $x_0(\mu, 0)$. (*b*) Same elliptic OECSs as (*a*), along with the singularities of the underlying tensor field $S(x, t)$. (Online version in colour.)

null geodesics as they contain more than two wedges in their interiors. By contrast, they are identified by the method we developed here.

Appendix B. Steps for the computation of closed null geodesics

Algorithm 1 provides a brief summary of the main steps performed by the MATLAB code (see the electronic supplementary material) for the computation of closed null geodesics. Specifically, algorithm 1 computes elliptic LCSs. We list the *MATLAB subfunctions* used to compute the formulae in §4.

Algorithm 1. Compute elliptic LCSs (see §4).

Input: (i) Entries of the Cauchy–Green tensor field $C^{ij}(x)$ and their spatial derivatives $C^{ij}_{x_k}(x),\ i, j, k \in \{1, 2\}$, along with the corresponding spatial grid vectors $xi\_g,\ i \in \{1, 2\}$. (ii) A vector $lamV$ containing the desired values of the parameter λ.

(i) Compute $\mathcal{R}_\lambda(0)$ (see equation (4.16)): *r0_lam.m*
(ii) Compute $\phi'(x_1, x_2, \phi)$ (see equation (4.15)): *Phi_prime.m*
(iii) Find closed null geodesics (see equations (4.15) and (4.16)): *FindClosedNullGeod.m*
(iv) Find outermost closed null geodesics: *FindOutermost.m*

Output: Elliptic LCSs corresponding to the different values of λ.

Algorithm 1 is general and can be used to compute elliptic OECSs (see §4) or any general closed null geodesics as defined in theorem 3.2, where $C^{ij}(x) = A^{ij}(x),\ i, j \in \{1, 2\}$. Steps (ii) and (iii) of algorithm 1 can be used to compute general non-closed null geodesics of Lorentzian metrics of the form $A_\alpha = A(x) - \alpha I$, such as hyperbolic and parabolic CSs, from given initial conditions.

Appendix C. Domain of existence of the reduced geodesic flow

Equation (3.7) only admits non-degenerate $r(s)=(x(s),\phi(s))^\top$ solutions in the set $V\subset U\times\mathbb{S}^1$: $B(x,\phi):=\langle e_\phi, R^\top A(x)e_\phi\rangle\neq 0$. Note that in the set $\bar{V}$ where $B(x,\phi)=0$, equation $g_x(e_\phi,e_\phi)=0$ (see equation (3.2)) does not define locally a two-dimensional manifold parametrized by $(x,\phi(x))$. In fact, by the implicit function theorem, $\phi(x)$ is defined only if $g_x(e_\phi,e_\phi)=0$ admits a solution and $\partial_\phi g_x(e_\phi,e_\phi)\neq 0$, where

$$\begin{aligned}\partial_\phi g_x(e_\phi,e_\phi)&=\tfrac{1}{2}\langle e_\phi, R^\top A(x)e_\phi\rangle+\tfrac{1}{2}\langle e_\phi, A(x)Re_\phi\rangle\\&=\langle e_\phi,\mathrm{Sym}(R^\top A(x))e_\phi\rangle=\langle e_\phi,R^\top A(x)e_\phi\rangle.\end{aligned}$$

Therefore, the set $\overline{V}$ is the union of points that satisfy at least one of the two following conditions:

$$\begin{aligned}&B(\cdot,\phi)=0\iff e_\phi\equiv\zeta_i(\cdot),\quad A(\cdot)\zeta_i(\cdot)=\alpha_i(\cdot)\zeta_i(\cdot),\quad \alpha_i(x)\in\mathbb{R},\ i=\{1,2\},\\&B(\phi,\cdot)=0\iff A(\cdot)\text{ is degenerate.}\end{aligned}$$

Equivalently,

$$V=\{(x,\phi)\in U\times\mathbb{S}^1: A(x)e_\phi\nparallel e_\phi,\ A(x)\neq\mathbf{0}\}.$$

Geometrically this means that, in $\overline{V}$, there cannot be a transverse zero of the function $g_x(e_\phi,e_\phi)$. Specifically, when the first condition holds, such zero is non-transverse at x only for the directions $\phi(x)$ aligned with the eigenvectors of $A(x)$. When the second condition holds, there cannot be any transverse zero at x for all ϕ, as $A(x)$ is degenerate and no distinguished directions exist.

Appendix D

(a) Hamiltonian reduction of the geodesic flow

Here we use the Hamiltonian formalism to derive a reduced geodesic flow which is equivalent to the one derived in §§2–3. With the generalized momentum p defined as

$$p=\frac{\partial L}{\partial x'}=A(x)x',\tag{D 1}$$

the parametrization $x(s)$ of a geodesic γ of the metric $g_x(v,v)=\frac{1}{2}\langle v,A(x)v\rangle$ satisfies the first-order system of differential equations

$$\left.\begin{aligned}&x'=A^{-1}(x)p\\\text{and}\qquad&p'=-\tfrac{1}{2}\nabla_x\langle p,A^{-1}(x)p\rangle,\end{aligned}\right\}\tag{D 2}$$

which is a canonical Hamiltonian system with Hamiltonian

$$H(x,p)=\tfrac{1}{2}\langle p,A^{-1}(x)p\rangle=L(x,x').\tag{D 3}$$

This Hamiltonian is constant along all geodesics of the metric g_x. In particular, if g_x is Lorentzian, then null geodesics of g_x lie in the zero-level surface of $H(x,p)$. As in §3, we derive a reduced form of the Hamiltonian flow (D 2), which is often referred to as the co-geodesic flow [27].

(b) Hamiltonian reduction to a three-dimensional geodesic flow

We introduce polar coordinates in the p direction by letting

$$p=\rho e_\phi,\quad \rho\in\mathbb{R}^+,\quad e_\phi=(\cos\phi,\sin\phi)^\top,\quad \phi\in\mathbb{S}^1.$$

We then rewrite equation (D 2) as

$$\left.\begin{aligned}&x'=\rho A^{-1}(x)e_\phi\\\text{and}\qquad&\rho' e_\phi+\phi'\rho Re_\phi=-\rho^2\tfrac{1}{2}\nabla_x\langle e_\phi,A^{-1}(x)e_\phi\rangle\end{aligned}\right\}\tag{D 4}$$

that, together with the rescaling (3.6), gives

$$\left.\begin{aligned} \frac{\mathrm{d}x}{\mathrm{d}\bar{s}} &= A^{-1}(x)e_\phi \\ \text{and}\qquad \frac{\mathrm{d}\rho}{\mathrm{d}\bar{s}}\rho e_\phi + \frac{\mathrm{d}\phi}{\mathrm{d}\bar{s}}\rho^2 Re &= -\rho^2\frac{1}{2}\nabla_x\langle e_\phi, A^{-1}(x)e_\phi\rangle, \end{aligned}\right\} \tag{D 5}$$

or, equivalently,

$$\left.\begin{aligned} \frac{\mathrm{d}x}{\mathrm{d}\bar{s}} &= A^{-1}(x)e_\phi, \\ \frac{\mathrm{d}\phi}{\mathrm{d}\bar{s}} &= -\frac{1}{2}\langle\nabla_x\langle e_\phi, A^{-1}(x)e_\phi\rangle, Re_\phi\rangle \\ \text{and}\qquad \frac{\mathrm{d}\rho}{\mathrm{d}\bar{s}} &= -\rho\frac{1}{2}\langle\nabla_x\langle e_\phi, A^{-1}(x)e_\phi\rangle, e_\phi\rangle. \end{aligned}\right\} \tag{D 6}$$

For any $\rho > 0$, system (D 6) has a three-dimensional reduced flow

$$\left.\begin{aligned} \frac{\mathrm{d}x}{\mathrm{d}\bar{s}} &= A^{-1}(x)e_\phi \\ \text{and}\qquad \frac{\mathrm{d}\phi}{\mathrm{d}\bar{s}} &= -\frac{1}{2}\langle\nabla_x\langle e_\phi, A^{-1}(x)e_\phi\rangle, Re_\phi\rangle. \end{aligned}\right\} \tag{D 7}$$

Therefore, any solution of (D 2) with $\rho > 0$ admits a projected flow of the form (D 7). This is due to the existence of a global invariant foliation in (D 6) that renders the (x, ϕ) coordinates of solutions independent of the evolution of their ρ coordinate. Closed orbits of (D 7) are, therefore, closed geodesics on (U, g_x), even though they may not be closed orbits of the full (D 6). Note that the ϕ component in equation (D 7) is the polar angle of the generalized momentum (see equation (D 1)), which is different from the ϕ in equation (3.7). Equation (D 7) does not appear to be available in the literature. The use of the energy (as opposed to the momentum p) as a coordinate appears in [28] in the context of perturbations of closed geodesics by time-periodic potentials. The reduced flow (D 7) in the (x, p) coordinates is equivalent to the reduced flow (3.7) in the (x, v) coordinates.

Geodesics can also be viewed as trajectories of (D 2) contained in a constant-level surface of the Hamiltonian $H(x, p)$. Null geodesics, in particular, are contained in the level surface

$$E_0 = \{(x, p) \in U \times \mathbb{R}^2 : H(x, p) = 0\},$$

which in polar coordinates, for any $\rho > 0$, can be rewritten as

$$E_0 = \{(x, \phi) \in U \times \mathbb{S}^1 : H(x, \phi) = \tfrac{1}{2}\langle e_\phi, A^{-1}(x)e_\phi\rangle = 0\}.$$

Finally, one should select the initial conditions for the ODE (D 7) as $x(0) = x_0$ and $\phi(0) = \phi_0$ on E_0 to satisfy $\langle e_{\phi_0}, A^{-1}(x_0)e_{\phi_0}\rangle = 0$.

References

1. Chakraborty P, Balachandar S, Adrian RJ. 2005 On the relationships between local vortex identification schemes. *J. Fluid Mech.* **535**, 189–214. (doi:10.1017/S0022112005004726)
2. Haller G. 2005 An objective definition of a vortex. *J. Fluid Mech.* **525**, 1–26. (doi:10.1017/S0022112004002526)
3. McWilliams JC. 1984 The emergence of isolated coherent vortices in turbulent flow. *J. Fluid Mech.* **146**, 21–43. (doi:10.1017/S0022112084001750)
4. Okubo A. 1970 Horizontal dispersion of floatable particles in the vicinity of velocity singularities such as convergences. *Deep Sea Res. Oceanogr.* **17**, 445–454. (doi:10.1016/0011-7471(70)90059-8)
5. Provenzale A. 1999 Transport by coherent barotropic vortices. *Annu. Rev. Fluid Mech.* **31**, 55–93. (doi:10.1146/annurev.fluid.31.1.55)
6. Weiss J. 1991 The dynamics of enstrophy transfer in two-dimensional hydrodynamics. *Physica D* **48**, 273–294. (doi:10.1016/0167-2789(91)90088-Q)

7. Blazevski D, Haller G. 2014 Hyperbolic and elliptic transport barriers in three-dimensional unsteady flows. *Physica D* **273**, 46–62. (doi:10.1016/j.physd.2014.01.007)
8. Farazmand M, Blazevski D, Haller G. 2014 Shearless transport barriers in unsteady two-dimensional flows and maps. *Physica D* **278**, 44–57. (doi:10.1016/j.physd.2014.03.008)
9. Haller G, Beron-Vera FJ. 2013 Coherent Lagrangian vortices: the black holes of turbulence. *J. Fluid Mech.* **731**, R4. (doi:10.1017/jfm.2013.391)
10. Oettinger D, Blazevski D, Haller G. 2016 Global variational approach to elliptic transport barriers in three dimensions. *Chaos* **26**, 033114. (doi:10.1063/1.4944732)
11. Oettinger D, Haller G. 2016 An autonomous dynamical system captures all LCSs in three-dimensional unsteady flows. *Chaos* **26**, 103111. (doi:10.1063/1.4965026)
12. Serra M, Haller G. 2016 Objective Eulerian coherent structures. *Chaos* **26**, 053110. (doi:10.1063/1.4951720)
13. Haller G. 2015 Lagrangian coherent structures. *Annu. Rev. Fluid Mech.* **47**, 137–162. (doi:10.1146/annurev-fluid-010313-141322)
14. Serra M, Haller G. 2016 Forecasting long-lived Lagrangian vortices from their objective Eulerian footprints. *J. Fluid Mech.* **813**, 436–457. (doi:10.1017/jfm.2016.865)
15. Hadjighasem A, Haller G. 2016 Level set formulation of two-dimensional Lagrangian vortex detection methods. *Chaos* **26**, 103102. (doi:10.1063/1.4964103)
16. Farazmand M, Haller G. 2012 Computing Lagrangian coherent structures from their variational theory. *Chaos* **22**, 013128. (doi:10.1063/1.3690153)
17. Tchon KF, Dompierre J, Vallet MG, Guibault F, Camarero R. 2006 Two-dimensional metric tensor visualization using pseudo-meshes. *Eng. Comput.* **22**, 121–131. (doi:10.1007/s00366-006-0012-3)
18. Karrasch D, Huhn F, Haller G. 2015 Automated detection of coherent Lagrangian vortices in two-dimensional unsteady flows. *Proc. R. Soc. A* **471**, 20140639. (doi:10.1098/rspa.2014.0639)
19. Delmarcelle T. 1994 The visualization of second-order tensor fields. PhD thesis, Stanford University Stanford, CA, USA.
20. Gelfand IM, Fomin S. 2000 *Calculus of variations*. New York, NY: Dover Publications.
21. Ying L, Candes EJ. 2006 Fast geodesics computation with the phase flow method. *J. Comput. Phys.* **220**, 6–18. (doi:10.1016/j.jcp.2006.07.032)
22. Truesdell C, Noll W. 2004 *The non-linear field theories of mechanics*. Berlin, Germany: Springer.
23. Haller G, Beron-Vera FJ. 2012 Geodesic theory of transport barriers in two-dimensional flows. *Physica D* **241**, 1680–1702. (doi:10.1016/j.physd.2012.06.012)
24. Wang Y, Olascoaga MJ, Beron-Vera FJ. 2015 Coherent water transport across the South Atlantic. *Geophys. Res. Lett.* **42**, 4072–4079. (doi:10.1002/2015GL064089)
25. Beron-Vera FJ, Wang Y, Olascoaga MJ, Goni GJ, Haller G. 2013 Objective detection of oceanic eddies and the Agulhas leakage. *J. Phys. Oceanogr.* **43**, 1426–1438. (doi:10.1175/JPO-D-12-0171.1)
26. Eberly D. 1996 *Ridges in image and data analysis*, vol. 7. Berlin, Germany: Springer.
27. Klingenberg WPA. 1995 *Riemannian geometry*, vol. 1. Berlin, Germany: Walter de Gruyter.
28. Delshams A, de la Llave R, Seara MT. 2000 Geometric approach to the existence of orbits with unbounded energy in generic periodic perturbations by a potential of generic geodesic flows of T2. *Commun. Math. Phys.* **209**, 353–392. (doi:10.1007/PL00020961)